

# Variations of Airflow and Electric Fields in a Corona Device During Charging of a Moving Dielectric Substrate

Parsa Zamankhan and Goodarz Ahmadi

Department of Mechanical and Aeronautical Engineering, Clarkson University, Potsdam,  
New York 13699-5725  
E-mail: ahmadi@clarkson.edu

Fa-Gung Fan

J.C. Wilson Center for Research and Technology, Xerox Corporation, Webster, New York 14580

---

**Abstract.** *The steady state airflow and electric field distributions in a corona device (corotron) during charging of a moving dielectric substrate (photoreceptor) for different operating conditions are studied. The set of two-way, fully coupled electrohydrodynamics governing equations is used in the analysis and parametric studies are performed. The effects of wire voltage, photoreceptor speed, and device-substrate gap size on photoreceptor charging, airflow, charge density, and electrical potential are studied. It is shown that the charging is strongly affected by the wire voltage and the substrate speed. The results also show the importance of corona wind effect on the flow structure in the device. © 2006 Society for Imaging Science and Technology.*

[DOI: 10.2352/J.ImagingSci.Technol.(2006)50:4(375)]

---

## INTRODUCTION

Corotrons are devices that are essential for the operation of electrophotographic machines and xerography process.<sup>1</sup> They are used for charging the photoreceptor and the paper surfaces to desired voltage levels for the purpose of toner transfer. A typical corotron is a long rectangle box with all its sides grounded except the side facing the photoreceptor. One or several thin wires located inside the corotron serve as the corona generating elements. During the operation of a simple direct current (dc) corotron, a high voltage is applied to the wires. Corona discharge occurs when the intensity of the electric field near the wire exceeds the threshold of air breakdown. The gas molecules near the wire in a region called “ionized sheath” are ionized. The wire then attracts the opposite polarity ions and repels the same polarity ones. A unipolar charge current is then generated from the wire to the shield and the substrate.

The amount of surface charge received by the moving substrate (photoreceptor) depends on the corotron size, wire voltage, gap size, and substrate speed, among others. To achieve a proper value of surface charge, detailed knowledge of the electrical quantities is necessary. While electrical quantities control the charging processes, understanding airflow condition is also very important. This is because the airflow in and around a corona device has major impacts on

the device contamination (e.g., due to particles, dust) and the emission of corona effluents (e.g., ozone, NO<sub>x</sub>).

Corona discharges in wire-plate and wire-shield geometries, including the electrostatic precipitator and high voltage dc transmission lines, were studied numerically and experimentally by several authors.<sup>2–16</sup> Most earlier studies were focused on the electrical quantities.<sup>2–11</sup> A few also addressed the hydrodynamical flow properties<sup>12–14</sup> of these devices. More recently the electrical and hydrodynamical coupling of the electrohydrodynamic (EHD) flows has received increasingly more attention.<sup>15,16</sup>

Various numerical methods have been used in modeling electrohydrodynamics in the past. In Refs. 2 and 13 finite difference methods were used, while finite element methods were employed in the work of Refs. 3 and 4 and Refs. 15 and 16. A combination of finite element and finite difference approach was used in Refs. 5 and 14. Earlier, the method of characteristic was used in Refs. 6–8 and finite volume methods were implemented in Refs. 9 and 10 for solving the electrostatics equations.

While there are many numerical and experimental studies of electrostatic precipitators and high voltage dc transmission lines, there is very little work on corotron charging against a moving dielectric substrate. The recent work of Feng et al.<sup>17</sup> for a steady state electric field in a corotron is an exception. They, however, ignored the airflow and simulated the corona charging with a finite element method. Feng et al.<sup>17</sup> also favorably compared their numerical and experimental results.

In this paper, the steady state electric and airflow fields in a corotron with a moving photoreceptor are analyzed. The fully coupled electrohydrodynamic governing equations are solved with a finite element method through FIDAP™ (Ref. 18) commercial software code. For different operating conditions, the electrical and hydrodynamical field quantities in and around the corotron are evaluated. For the case where the airflow is absent, the simulation results are compared with those of Feng et al.<sup>17</sup> and good agreement is observed. A series of coupled flow and electric fields analyses show that the corona discharge creates strong corona wind in the corotron. The results also show that the wire voltage,

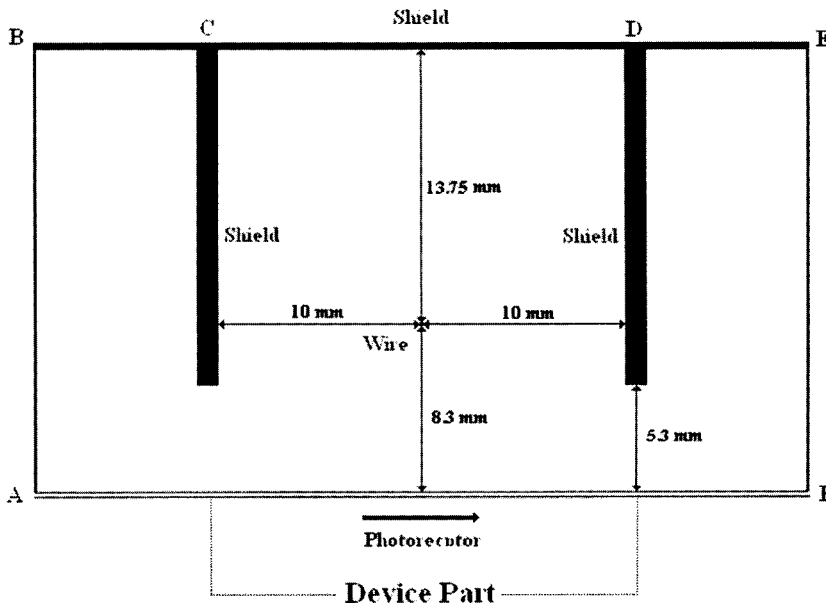


Figure 1. Schematic of cross section of the corotron and the computational domain.

the gap size, and the substrate speed have profound effects on the airflow field in the corotron.

**GOVERNING EQUATIONS**

In this section the governing equations of coupled electrohydrodynamic flow in a corotron are presented. The speed of the photoreceptor in high-speed electrophotographic machines typically travels around 0.5 m/s or less. Corona airflow due to the wire discharge produces a velocity that could reach up to about 2 m/s in some regions inside of the corotron. The corresponding Reynolds number based on the width of the corotron is typically much smaller than the critical Reynolds number for turbulence in a cavity flow; therefore, the air flow in the device is assumed to be in laminar flow regime. In this study it is also assumed that the polarity of the wire is positive and the discharge is uniform along the wire so the negative corona instabilities are not induced into the flow. Since the dimension of a corotron along its wire direction is much larger than its cross section, a two-dimensional model is considered to be sufficient in the analysis. For constant material properties, the governing equations for a steady state two-dimensional electrohydrodynamic flow are given as

Gauss' law

$$\nabla^2 V = - \frac{q}{\epsilon_0}, \tag{1}$$

Conservation of charge:

$$\nabla \cdot (\mathbf{u}q) = D\nabla^2 q + b \nabla \cdot (q \nabla V), \tag{2}$$

Electric field-electrical potential relation:

$$\mathbf{E} = - \nabla V, \tag{3}$$

Continuity:

$$\nabla \cdot \mathbf{u} = 0, \tag{4}$$

Conservation of momentum:

$$\mathbf{u} \cdot \nabla \mathbf{u} = - \frac{1}{\rho} \nabla p + \nu \nabla^2 \mathbf{u} + q\mathbf{E}. \tag{5}$$

In Eqs. (1)–(5),  $V$  is the electrical potential,  $\mathbf{E}$  is the electric field vector,  $q$  is the space charge density,  $D$  is ion diffusivity in the air,  $b$  is the ion mobility, which is the ratio of the ion velocity in the field direction to the magnitude of the electric field,  $\epsilon_0$  is the air permittivity,  $p$  is the fluid pressure,  $\mathbf{u}$  is the fluid velocity vector,  $\rho$  is the fluid density, and  $\nu$  is the kinematic viscosity. It should be emphasized that the conservation of charge given by Eq. (2) includes the charge transport by ion mobility as well as the convective transport by airflow and the molecular diffusion.

**GEOMETRY**

Figure 1 shows schematically the cross section of a corotron consisting of a single thin wire, three grounded shield plates and a moving substrate (photoreceptor). The relevant dimensions are also shown in this figure. The modeled computational domain includes the surrounding region exterior to the device so that more realistic boundary conditions can be prescribed.

As noted above, when a high voltage is applied to the wire and the intensity of the electric field near the wire exceeds the air breakdown threshold, the air molecules near to the wire are ionized, and a corona current from the wire initiates. Part of the current is directed toward the photoreceptor and charges up its surface. That is during the time under the corotron, charges are accumulated on substrate surface due to exposure to the charge flow. As charge builds up on a surface segment, it will increasingly repel the ions so the charging rate decreases as the surface segment moves toward the corotron exit.

Due to the movement of the ions (corona wind), the air experiences an effective electrical body force. This electrical body force in addition to the viscous forces induced by the moving photoreceptor creates a rather complex flow pattern in the corotron. Understanding the flow structure under different operating condition is important for contaminant transport and control and for increasing the performance and the life of corotron devices.

In the performed simulations a permittivity of  $\epsilon_0 = 8.85 \times 10^{-12} \text{ C}^2/\text{N m}^2$ , an ion mobility of  $b = 2 \times 10^{-4} \text{ m}^2/\text{V s}$ , an ion diffusivity of  $D = 5.32 \times 10^{-6} \text{ m}^2/\text{s}$ , and an air viscosity of  $\mu = 1.84 \times 10^{-5} \text{ N s/m}^2$  are assumed.

### BOUNDARY CONDITIONS

For the corotron geometry shown in Fig. 1, the hydrodynamical boundary conditions are

$$\text{at the shields (wall): } u = 0, \quad (6)$$

$$\text{at the wire surface: } u = 0, \quad (7)$$

$$\text{along } A-B \text{ and } E-F: \frac{\partial u_x}{\partial x} = 0, \quad (8)$$

$$\text{along } B-C \text{ and } D-E: \frac{\partial u_y}{\partial y} = 0, \quad (9)$$

$$\text{at the substrate } u_x = \text{substrate speed, } u_y = 0. \quad (10)$$

Electrical boundary conditions used are

$$\text{at the wire surface: } V = V_0, \quad (11)$$

$$\text{at the shields: } V = 0, \frac{\partial q}{\partial n} = 0, \quad (12)$$

$$\text{along } A-B, B-C, D-E, \text{ and } E-F: \frac{\partial V}{\partial n} = 0, \frac{\partial q}{\partial n} = 0, \quad (13)$$

$$\text{at the substrate: } \frac{\partial q}{\partial n} = 0. \quad (14)$$

In Eqs. (12)–(14),  $n$  represents the local unit normal outward from the modeled domain.

Since ion transport by diffusion is included in the charge conservation equation given by Eq. (2), boundary conditions at all the boundaries are required. The details of the physical situation for the space charge at the solid boundaries such as the shields and the substrate are not known. Feng<sup>15</sup> and Medlin et al.,<sup>3</sup> used the zero gradient boundary condition on the walls. Feng et al.<sup>17</sup> used the same boundary condition for the shields and the substrate in corotron. Since the diffusion term in the charge transport equation is small comparing to the drift term, no noticeable

difference of their results with those<sup>2,5,6,8,13,14</sup> obtained for the cases that the diffusion term was neglected was observed. Therefore, in this study boundary condition given by Eqs. (12) and (14) are used.

The boundary conditions for the charge density at the wire and voltage at the substrate need more discussion. To estimate the charge density on the surface of a coronating wire, the Kaptsov's<sup>19</sup> assumption is used. Kaptsov's assumption relates the gradient of electrical potential at the wire surface to an onset field strength. That is,

$$\mathbf{n} \cdot \nabla V = \text{Constant} = E_{\text{onset}}, \quad (15)$$

where  $\mathbf{n}$  is the local unit normal vector that points into the wire,  $\nabla V$  is the gradient of potential on the wire surface, and  $E_{\text{onset}}$  is the electric field threshold strength for the corona onset. Here  $E_{\text{onset}}$  can be calculated from Peek's formula<sup>20</sup> given as

$$E_{\text{onset}} = \left( A \delta + B \sqrt{\frac{\delta}{R_w}} \right). \quad (16)$$

In Eq. (16)  $R_w$  is the radius of the wire,  $\delta$  is the gas density considered as  $1.225 \text{ kg/m}^3$  in this study, and  $A = 32.3 \times 10^5 \text{ V/m}$ ,  $B = 8.46 \times 10^4 \text{ V/m}^{1/2}$  are the constants of Peek's formula.

Based on Peek's formula given by Eq. (16), an iterative procedure for applying the charge density boundary condition on the wire was developed. A value for the charge density on each node on the wire surface was first estimated. Then the value of  $\mathbf{n} \cdot \nabla V$  for each node of the wire surface was calculated and compared with  $E_{\text{onset}}$ , which was obtained from Eq. (16). If the difference between the value of  $\mathbf{n} \cdot \nabla V$  and  $E_{\text{onset}}$  for any node on the wire was larger than a prescribed tolerance, new corrected values for the charge density on each node on the wire were evaluated and the governing equation were solved again. This iterative procedure was repeated until the difference between the value of  $\mathbf{n} \cdot \nabla V$  and  $E_{\text{onset}}$  for all nodes on the wire became smaller than the prescribed tolerance.

To estimate the new values for the charge density on each node on the wire (after a block of ten iterations) the new estimate for the value of charge density on the wire was evaluated using

$$q_{w\text{-New}} = (1 - \alpha)q_{w\text{-old}} + \alpha q_w^*, \quad (17)$$

where

$$q_w^* = q_{w\text{-old}} \left( \frac{\mathbf{n} \cdot \nabla V}{E_{\text{onset}}} \right)^p. \quad (18)$$

In Eqs. (17) and (18),  $q_{w\text{-old}}$  is the old value of the charge density on the wire that is being updated by the ratio of  $(\mathbf{n} \cdot \nabla V / E_{\text{onset}})^p$  for evaluating  $q_w^*$ .

To avoid sharp changes in the value of charge density that could drive the solution to diverge, the under-relaxation factor,  $\alpha$ , was introduced in Eq. (17). In the beginning of iteration, a value of  $\alpha = 0.3$  and  $p = 1$  was used. As the itera-

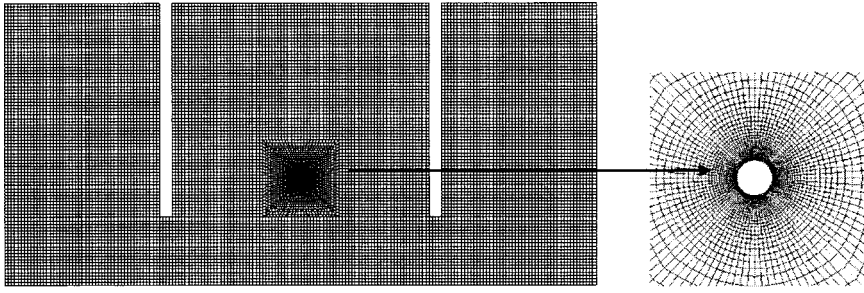


Figure 2. Computational grid.

tion progressed,  $\alpha$  was gradually increased to 1 and the value of  $p$  was also subsequently increased to 4 so that a faster convergence can be obtained. In the present simulation, a tolerance of  $0.000\ 01 E_{\text{onset}}$  for condition (15) was used. For the cases studied, it was found that decreasing the tolerance from this level to  $5 \times 10^{-6} E_{\text{onset}}$  had negligible effects on the profile of the wire charge density. Therefore, it was concluded that the assumed tolerance was sufficient. To implement this procedure, user defined subroutines for FIDAP<sup>TM</sup> were developed and used in the simulation.

Care should be given in applying this procedure during the simulation. We found that the structure of the mesh near the wire could significantly affect the convergence of the solution in FIDAP<sup>TM</sup>. That is, the presence of skewed mesh near the corona wire causes the values of  $E_{\text{normal}}$  on the wire nodes to oscillate and do not converge to proper values. This in turn leads to unrealistic distribution of charge density on the wire. To avoid this problem, as shown in the magnified region near the wire in Fig. 2, a larger circular region around the wire was created in the computation domain. The generated mesh in this region was made fine and symmetric. As a result of using this symmetric and refined mesh near the wire, satisfying the Kaptsov's condition for the wire nodes was achieved with no problem in for the all cases studied.

The voltage boundary condition on the moving photoreceptor follows from the conservation of surface charge on the moving photoreceptor surface. Accordingly, in the steady-state condition the surface charge conservation may be expressed as

$$u_{\text{ph}} \frac{\partial \sigma}{\partial x} = bq \frac{\partial V}{\partial y}. \tag{19}$$

In Eq. (19)  $u_{\text{ph}}$  is the photoreceptor speed and  $\sigma$  is the surface charge density on the photoreceptor. Since the pho-

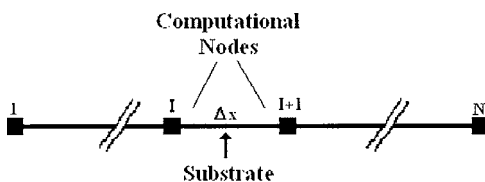


Figure 3. Schematic of computational grids at the photoreceptor surface for evaluating the voltage boundary condition.

toceptor thickness is very small, surface charge may be related to its local voltage as

$$\sigma = \epsilon_0 \frac{V}{t_d / \kappa}. \tag{20}$$

In Eq. (20),  $t_d$  is the photoreceptor thickness and  $\kappa$  is the photoreceptor dielectric constant. Equation (20) follows from Gauss law as described by Feng et al.<sup>17</sup> (The derivation of Eq. (20) is given in as Supplemental Material on the ISBT website, www.imaging.org.)

Using Eq. (20) in Eq. (19), the voltage boundary condition for the photoreceptor is given as

$$\frac{\partial V}{\partial x} = \frac{(bqt_d / \kappa) \partial V}{u_{\text{ph}} \epsilon_0 \partial y}. \tag{21}$$

Assuming that the photoreceptor voltage at point A in Fig. 1 is zero, Eq. (21) is integrated along the photoreceptor using the mesh shown in Fig. 3. The voltage at different nodes at the surface of the photoreceptor is given as

$$V(I+1) = b \frac{qt_d / \kappa}{u_{\text{ph}} \epsilon_0} \Delta x + V(I). \tag{22}$$

With Eq. (22) for the voltage boundary condition on the photoreceptor, the set of boundary conditions needed for solving the governing equations becomes complete. During the simulation, after each block of ten iterations, in addition to the charge density profile on the wire the voltage profile on the photoreceptor surface is also updated using Eq. (22). Unless stated otherwise, in the present simulations,  $t_d = 25 \mu\text{m}$  and  $\kappa = 3.3$  are used. A user defined subroutine was also developed for implementing Eq. (22) in the FIDAP<sup>TM</sup> code.

**NUMERICAL SCHEME**

Since the finite element formulation in FIDAP<sup>TM</sup> code uses the standard Galerkin method as default, care needs to be given to the value of nodal electrical Peclet number for the charge transport equation. The electrical Peclet number is defined as

**Table 1.** Exit voltage of photoreceptor and the current per unit length at the wire in comparison with the experimental data of Feng *et al.* (see Ref. 17). The photoreceptor speed is 0.5 m/s.

Wire voltage (V)	Exit voltage (V)				Current per unit length at the wire (mA/m)			
	Standard Galerkin	Upwind Petrov-Galerkin	Standard Galerkin with modified diffusivity	Experimental	Standard Galerkin	Upwind Petrov-Galerkin	Standard Galerkin with modified diffusivity	Experimental
4500	145.6	146.3	145.7	141	0.184	0.187	0.186	0.197
6000	660	672.7	663.8	672	1.016	1.025	1.025	1.096

$$Pe_E = \frac{U_E L}{D}. \quad (23)$$

In Eq. (23),  $U_E$  is the magnitude of the local ion drift velocity,  $L$  is the characteristic length of the element, and  $D$  is the ion diffusivity in the media. Here square root of the computational cell area is used for the characteristic length scale. The magnitude of ion drift velocity may also be evaluated as

$$U_E = \sqrt{\left(u_x - b \frac{\partial V}{\partial x}\right)^2 + \left(u_y - b \frac{\partial V}{\partial y}\right)^2}. \quad (24)$$

In Eq. (24),  $b$  is the ion mobility and  $V$  is the electrical potential.

Several authors include Zienkiewicz and Taylor<sup>21</sup> reported that high values of electrical Peclet number inherently create wiggling in the solution that could lead to divergence. Using high order elements (for example quadratic) or mesh refining can decrease the local electric Peclet number; however, these methods increase the computational time significantly. Increasing the diffusivity and using upwinding are the other alternatives for stabilizing the numerical process when the value of Peclet number is high in some part of the computational domain.

Zienkiewicz and Taylor<sup>21</sup> suggested that using the standard Galerkin method with a modified diffusivity given by

$$D_a = D + 0.5\beta Uh \quad (25)$$

for a one-dimensional advection-diffusion equation with constant advection velocity and constant grid size is equivalent to a finite element formulation based on Petrov-Galerkin method with  $\beta$  as a parameter. In Eq. (25),  $D_a$  is the modified diffusivity,  $D$  is the true diffusivity,  $U$  is the advection velocity, and  $h$  is the grid size. Here  $\beta=0$  is equivalent to the standard Galerkin formulation which neglects the convection effects; while  $\beta=1$  corresponds to the upwind Petrov-Galerkin method that is a pure convection formulation and neglects the diffusion. Since the effects of both diffusion and convection may be important, using  $\beta=0$  or 1 may not provide accurate results. Christie *et al.*<sup>22</sup> proved that in a one dimensional problem with constant

advection velocity and grid size, the optimal value for  $\beta$  is given by

$$\beta_{opt} = \coth(Pe) - \frac{1}{Pe}. \quad (26)$$

Although the cases studied in the present work are two dimensional with variable advection velocity and variable grid sizes, still the modified diffusivity as given by Eqs. (25) and (26) (with  $U$  and  $Pe$  replaced by  $U_E$  and  $Pe_E$ , respectively) may be more appropriate and could be used to improve the stability of the simulations.

Using the two-dimensional upwind Petrov-Galerkin formulation that has been provided in FIDAP<sup>TM</sup> is another approach that can handle the mentioned instability problem. The details of different discretization methods were given by Zienkiewicz and Taylor.<sup>21</sup> Additional references may be found in the FIDAP<sup>TM</sup> manual.<sup>18</sup> In the subsequent sections, the simulation results using the standard Galerkin, the standard Galerkin with a modified diffusivity, and the upwind Petrov-Galerkin schemes are compared with the experimental data of Ref. 17.

## COMPARISON WITH EXPERIMENT

Feng *et al.*<sup>17</sup> performed numerical and experimental studies of the electrical properties in a corotron which is identical to the one shown in Fig. 1 for different wire voltages and photoreceptor speeds. Since the charge transport by air flow was assumed negligible in comparison with the charge transport by electric fields, the contribution was not included in their simulations. The computational domain in the simulation of Feng *et al.*<sup>17</sup> also covered only the corotron (section *CD*) and did not include the surrounding area shown in Fig. 1.

For the conditions identical to those used by Feng *et al.*,<sup>17</sup> we have simulated the conditions in the corotron using the standard Galerkin, the standard Galerkin with modified diffusivity as given by Eqs. (25) and (26) and the upwind Petrov-Galerkin finite element approaches. The charge conservation equation without the convective charge transport term was used in these simulations. The computational mesh for this case contained 12840 linear elements. Since in this case the computational domain does not in-

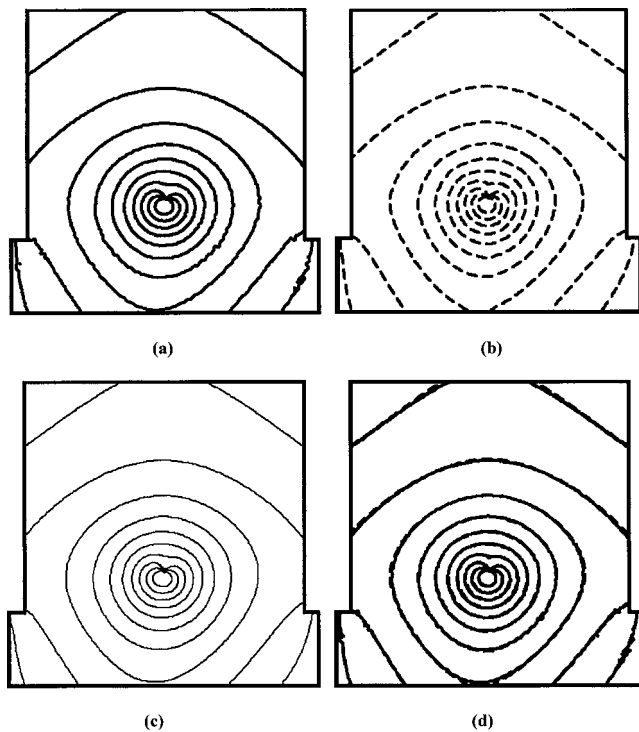


**Figure 4.** Charge density contours in the corotron for a wire voltage of 6000 V, photoreceptor speed as 0.5 m/s, and gap size of 5.3 mm simulated by different methods. Contours are from 0.15 to 1.2 mC/m<sup>3</sup> with an increment of 0.117 mC/m<sup>3</sup>. (a) Standard Galerkin. (b) Upwind Petrov-Galerkin. (c) Standard Galerkin with a modified diffusivity. (d) Comparison of different methods.

clude the region outside the corotron, boundary conditions (8), (9), and (13) are replaced by the zero gradients of electrical potential and charge density at the inlet and outlet gap between the corotron and photoreceptor surface. Simulations were performed for wire voltage of 4500 and 6000 V for a photoreceptor speed of 0.5 m/s and the results are compared with the experimental results reported by Feng et al.<sup>17</sup>

For the case that the wire voltage is 6000 V, Fig. 4 shows the charge density contours evaluated using different finite element schemes. It is seen that the predicted charge density contours are nearly the same; however, the standard Galerkin method shows some wiggling due to the high values of nodal electrical Peclet number.

Table I compares the exit voltage of the photoreceptor surface and the current density from the wire as predicted by different finite element approaches with the experimental data of Feng et al.<sup>17</sup> It is seen that the simulation results for the photoreceptor voltage and the wire current density are almost the same and are in good agreement with the experimental data.

Based on the simulations performed with different finite element methods, the Galerkin finite element method with the modified diffusivity was selected for analyzing of the electric and flow fields in the corotron in this study. The standard Galerkin method was discarded due to its inherent inability of handling high nodal electrical Peclet number

conditions. While the upwind Petrov-Galerkin method can also provide stable solution, it was not used because the current FIDAP<sup>TM</sup> implementation does not allow it to be generalized to include both the drift and the convective transports of ions.

#### IMPLEMENTATION IN FIDAP

FIDAP<sup>TM</sup> is a finite element code for solving the thermofluid transport processes including species transport equations. The code has the capability of handling EHD problems. The code default approach discretizes the governing equations using the standard Galerkin formulation; however, different version of the Petrov-Galerkin formulation can also be used. The details of different discretization methods were given by Zienkiewicz and Taylor.<sup>21</sup> Additional references may be found in the FIDAP<sup>TM</sup> manual.<sup>18</sup>

The discretized form of the governing equations can be solved by coupled or segregated solvers. In the coupled method the system of governing equations are solved simultaneously. In the segregated method, however, equations are solved consecutively. Coupled solvers are numerically more stable but they require more memory and computational time. In contrast, the segregated solvers need less memory and are faster but they are less stable. Both coupled and segregated solvers in FIDAP<sup>TM</sup> use the Gaussian elimination method by default. There are, however, other methods available. Information concerning these additional methods may be found in the FIDAP<sup>TM</sup> manual.<sup>18</sup>

In this study, for evaluation of the charge conservation equation given by (2), the standard Galerkin formulation with a modified diffusivity based on Eqs. (25) and (26) was used. The momentum equation was, however, discretized by the up-wind Petrov-Galerkin formulation as available in FIDAP<sup>TM</sup> to increase the stability of the numerical scheme. To solve the discretized system of equations, the segregated method using Gaussian elimination solver was used in the analysis.

Except for the charge density condition on the wire and voltage distribution on the photoreceptor, imposing the boundary conditions was straightforward and was performed directly in FIDAP<sup>TM</sup>. To impose the boundary conditions for the charge density on the wire and voltage on the photoreceptor, two FORTRAN codes based on the procedure described in Boundary Conditions section were developed and were implemented into a user-subroutine of the software.

It was found that the procedure was somewhat sensitive to the initial guess for the values of charge density on the wire in that a large overestimation by a factor of 10–20 may cause the solution to diverge. In those cases the computations were repeated with a smaller value of the initial guess.

Another modification of the FIDAP<sup>TM</sup> code was in the need for inclusion of the Coulomb force in the momentum equation through a user-defined subroutine. Here also it was found that the Coulomb force needs to be gradually introduced to avoid the risk of divergence of the solution.

The grid independency of the solutions was also checked. Typically the grid size was increase by a factor of

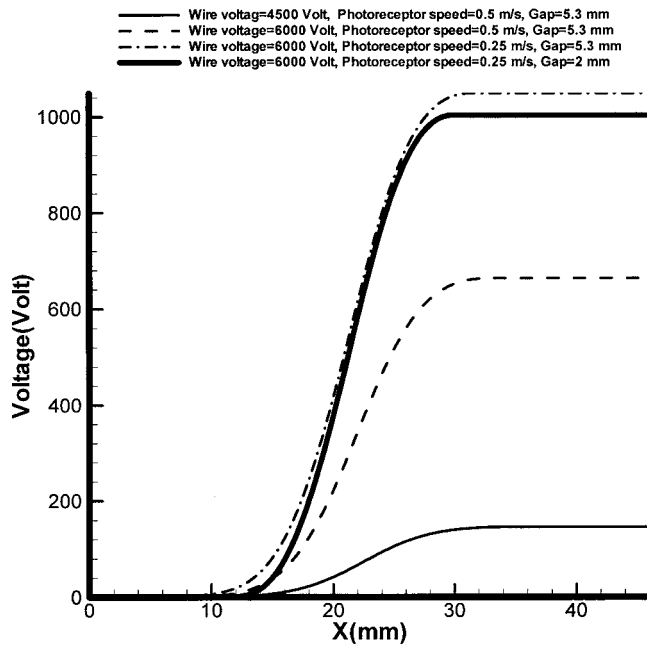


Figure 5. Voltage distribution on the photoreceptor for different cases (the device is located between  $x = 12$  and  $34$  mm).

50% and the solution was repeated until the difference in the solution was insignificant.

## RESULTS AND DISCUSSIONS

A series of simulations were performed and the effects of wire voltage, photoreceptor speed and the corotron-photoreceptor gap size on the photoreceptor charging, and the electric and flow fields in the corotron were studied. Here the fully coupled EHD governing equations including ion convection were used and the simulation results are presented and discussed. To provide a more accurate simulation of the flow field, the computational domain was extended to cover region beyond the corotron device. Figures 1 and 2, respectively, show the schematic of the computational domain and the computational mesh used in the analysis.

A corotron with the wire voltage of 6000 V, the photoreceptor speed of 0.5 m/s, and the gap size between the corotron and photoreceptor surface of 5.3 mm was considered as the reference case. A series of simulations were performed and the effect of variation in wire voltage, photoreceptor speed and gap size was studied. In one case the wire voltage was reduced to 4500 V, and in the other case the photoreceptor speed was reduced to 0.25 m/s, while all other conditions were kept fixed. For the case that the photoreceptor speed is 0.25 m/s, the effect of reduction of the gap size from 5.3 to 2 mm was also studied.

During the operation of device, charges are accumulated on the photoreceptor surface during its motion under the coronating wire due to exposure to the charge density current from the wire. As charge builds up on the moving photoreceptor surface, it will increasingly resist the approaching ions and the rate of charging decreases as the photoreceptor moves toward the outlet section of the device.

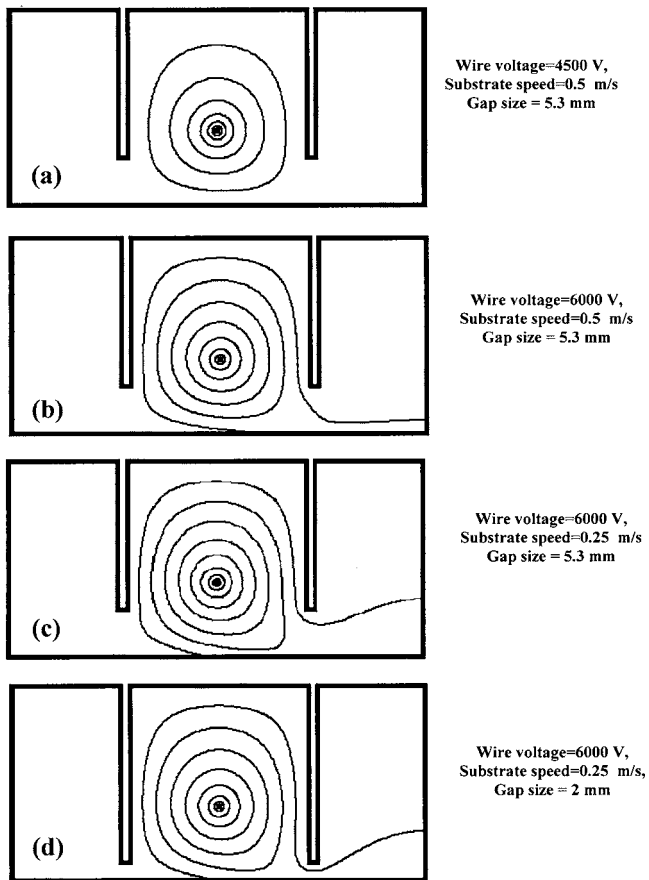
This process will eventually lead to the saturation of charge build up and the amount of surface charge on the photoreceptor surface reaches to a constant value near the corotron outlet. Since the surface charge is proportional to the voltage as given by Eq. (20), the distribution of voltage on the photoreceptor follows a similar distribution.

Figure 5 shows the computed distribution of the photoreceptor surface voltage for different operating conditions. In this figure the left and right edges of the corotron are, respectively, 12 and 34 mm. For different conditions, Fig. 5 shows that the trend of variation of the surface charging is the same, while the voltage amplitude differs significantly. It is also seen that the photoreceptor surface is being charged slightly even before it gets to the left edge of the corotron. The voltage begins to increase as the surface enters region directly under the corotron. The rate of charging and voltage build up is slow at the beginning but becomes quite steep with distance from the inlet. The voltage then builds up rapidly and saturates to a constant value. The maximum voltage acquired by the photoreceptor surface varies significantly depending on the corotron operating conditions. For a wire voltage of 4500 V, the photoreceptor reaches to about 146 V. For the reference case with a wire voltage of 6000 V, the photoreceptor voltage reaches to about 665 V. As expected, the increase of wire voltage significantly increases the amplitude of the photoreceptor surface charge and the corresponding voltage.

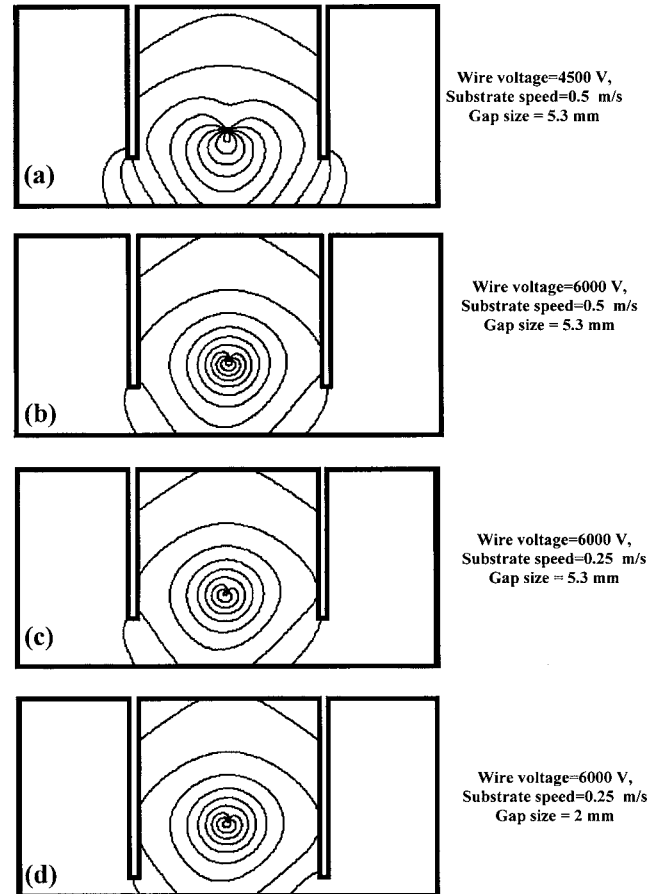
For the reference conditions, when the speed is reduced to 0.25 m/s, Fig. 5 shows that photoreceptor exit voltage increases to about 1050 V. That is, in agreement with Feng et al.,<sup>17</sup> at lower speeds the photoreceptor is exposed to the charge flow for a longer period and the charge buildup on the photoreceptor surface increases. The effect of reducing the gap size between the corotron and the photoreceptor to 2 mm on the surface charging could also be seen from Fig. 5. Here the wire voltage is 6000 V and the speed is 0.25 m/s. It is seen that decreasing the gap size leads to decrease of the photoreceptor voltage to about 1005 V.

Figure 6 shows the simulated electrical potential contours in the corotron for different cases. It is seen that the potential contours are roughly concentric circles around the wire. At higher wire voltage and lower photoreceptor speed, the contours become somewhat asymmetric tending to have higher values in the region near the outlet in comparison to the inlet side. The asymmetric becomes more noticeable as the wire voltage increases or the photoreceptor speed decreases. As was noted in the discussion of Fig. 5, increasing the wire voltage or decreasing the photoreceptor speed increases the nonuniformity of voltage on the photoreceptor surface leading to higher level of asymmetry in the potential contours. Figure 6 also shows that decreasing the gap size does not have a noticeable effect on the distribution of the electrical potential in the corotron.

Figure 7 shows the computed charge density contours in the corotron for different cases studied. This figure shows that the charge density is highest near the coronating wire and the contours are somewhat asymmetric in all the cases



**Figure 6.** Electrical potential contours for different cases. (a) Wire voltage of 4500 V, photoreceptor speed of 0.5 m/s, and gap size of 5.3 mm. (Minimum contour=450 V, increment 450 V.) (b) Wire voltage of 6000 V, photoreceptor speed of 0.5 m/s, and gap size of 5.3 mm. (c) Wire voltage of 6000 V, photoreceptor speed of 0.25 m/s, and gap size=5.3 mm. (d) Wire voltage of 6000 V, photoreceptor speed of 0.25 m/s, and gap size=2 mm. [For (b), (c), and (d) minimum contour=600 V, increment 600 V.]



**Figure 7.** Charge density contours for different cases. (a) Contours are from 0.029 to 0.29 mC/m<sup>3</sup> with an increment of 0.029 mc/m<sup>3</sup> for wire voltage of 4500 V, photoreceptor speed of 0.5 m/s, and gap size=5.3 mm. (b) Wire voltage of 6000 V, photoreceptor speed of 0.5 m/s, and gap size of 5.3 mm. (c) Wire voltage of 6000 V, photoreceptor speed of 0.25 m/s, gap size of 5.3 mm. (d) Wire voltage of 6000 V, photoreceptor speed of 0.25 m/s, and gap size=2 mm. For cases (b), (c), and (d), contours are from 0.15 to 1.3 mC/m<sup>3</sup> with an increment of 0.127 mC/m<sup>3</sup>.

studied. In particular, the asymmetry of the charge density near the wire is more noticeable. The asymmetric distribution of charge density is also due to the nonuniform distribution of the voltage on the photoreceptor surface. As the wire voltage increases or the photoreceptor speed decreases, the charge density contours become more asymmetric. Since the voltage in the region near the outlet is higher than that near the inlet, the ions face stronger resistance near the outlet and the charge density values drops in this region.

Figure 8 shows the charge density distribution on the wire for different operating conditions. It is seen that the charge density distribution on the wire is markedly nonuniform for all cases studied. For the reference case, when the wire voltage is 6000 V, the photoreceptor speed is 0.5 m/s, and the gap size is 5.3 mm, the amplitude of the charge density on the wire varies between 0.9 and 1.4 mC/m<sup>3</sup>, which is the maximum among the cases studied. In this case, the maximum value of the charge density on the wire occurs at  $\phi=250^\circ$ . When the wire voltage is reduced to 4500 V, while the photoreceptor speed and the gap size are kept

fixed, respectively, at 0.5 m/s and 5.3 mm, the amplitude of the charge density on the wire varies between 0.12 and 0.28 mC/m<sup>3</sup>, which is the lowest in comparison with the other cases studied. The maximum value of the charge density on the wire in this case occurs at  $\phi=262^\circ$ , which shows a shift toward the center compared to the reference case.

Figure 8 also shows that when the photoreceptor speed decreases from 0.5 to 0.25 m/s with same wire voltage and gap size, the amplitude of charge density at the wire varies between 0.9 and 1.2 mC/m<sup>3</sup>, which somewhat lower than the reference case. As noted before, reducing the photoreceptor speed leads to an increase in its voltage, and the photoreceptor more strongly resist to the corona ion flow. Thus, the current from the wire decreases as the photoreceptor speed decreases, which is in agreement with the observation of Feng et al.<sup>17</sup> For this case the maximum charge density on the wire occurs at  $\phi=230^\circ$ , which shows a 20° inclination toward the inlet side compared to the reference case.

Effects of variation in the gap size on the charge density at the wire surface can also be seen from Fig. 8. When the

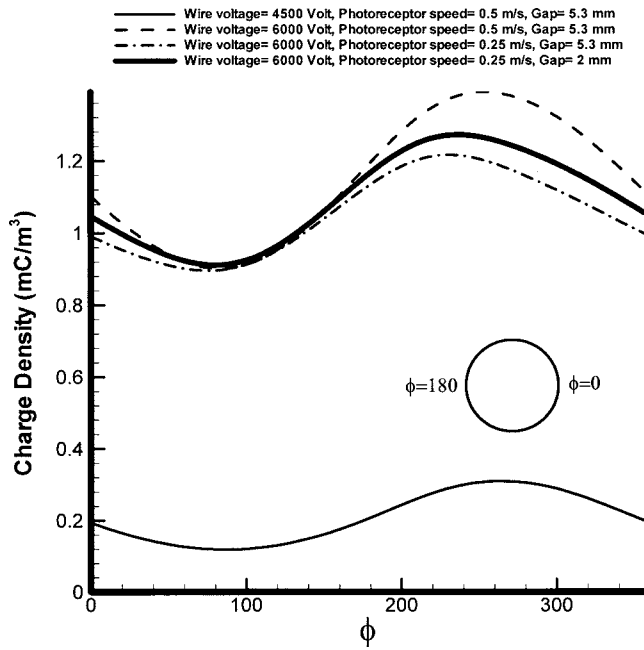


Figure 8. Charge density distribution at the wire surface for different cases.

wire voltage is 6000 V and the photoreceptor speed is 0.25 m/s, reducing the gap size to 2 mm, shows a slight increase in the charge density. In this case the amplitude of the charge density on the wire varies between 0.9 and 1.3 mC/m<sup>3</sup> with its maximum occurring at about  $\phi = 236^\circ$ . The slight increase of the charge density is due to the increase of the length of the side shields which decreases the total resistance of the corotron toward the ion injection.

When the gap size is decreased, Fig. 5 shows that the charge density current from the wire increases slightly, and the voltage amplitude of the photoreceptor somewhat decreases. This is perhaps due to the fact that some of the ions are attracted by the grounded shields instead of deposition on the highly charged regions of the photoreceptor near to the corotron outlet.

Figure 9 show the stream traces in and around the corotron for different cases. Here the wire size was exaggerated, and the stream traces were placed at locations to show the important features of the flow in the corotron. (It should be noted here that the concentration of stream traces in a region does not represent the velocity magnitude.) Figure 9(a) shows the corresponding stream traces for the case that the wire voltage is 4500 V, photoreceptor speed is 0.5 m/s, and the gap size is 5.3 mm. It is seen that the interaction of corona wind with the shear flow induced by the moving photoreceptor creates rather complex flow structures. A large clockwise vortex forms around the wire, which is extended from the top-left to the bottom-center of the corotron. Bulk of the flow entering the corotron by the motion of the photoreceptor from the left inlet, revolves around the large vortex, and leaves from the bottom part of the outlet section. This figure also shows a smaller counter-clockwise vortex forms near the outlet causing suction of air into the corotron

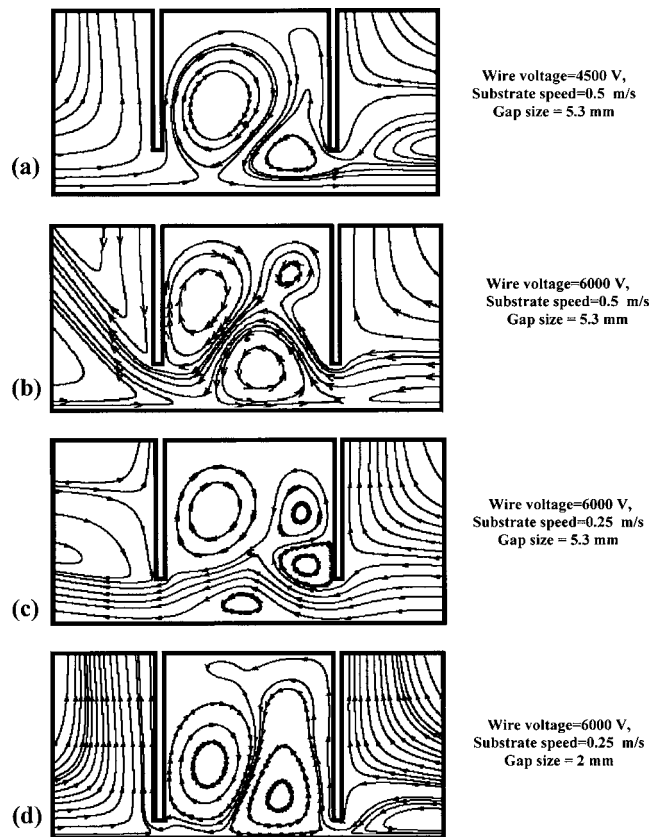


Figure 9. Stream traces for different cases. (a) Wire voltage=4500 V, photoreceptor speed=0.5 m/s, gap size=5.3 mm. (b) Wire voltage =6000 V, photoreceptor speed=0.5 m/s, gap size=5.3 mm. (c) Wire voltage=6000 V, photoreceptor speed=0.25 m/s, gap size =5.3 mm. (d) Wire voltage=6000 V, photoreceptor speed =0.25 m/s, gap size=2 mm.

from the top part of outlet section. This flow rotates around the small vortex and also leaves through the bottom part of the outlet section.

Figure 9(b) shows the stream-traces for the reference case with wire voltage of 6000 V, photoreceptor speed of 0.5 m/s, and the gap size of 5.3 mm. This figure shows that the clockwise vortex around the wire is still present but becomes smaller and shifts toward the inlet. The counter-clockwise vortex, which covers the right-lower part of the device becomes larger and moves toward the center. It is seen that air is sucked into the corotron from a large part of the outlet section and rotates around the central counter-clockwise vortex. There is also a smaller vortex forms on the top-right of the corotron, Fig. 9(b) shows that at high wire voltage the corona wind effects becomes very large and generates rather complex flow pattern in the corotron.

Figure 9(c) shows the stream traces for a case that the wire voltage is 6000 V, the gap size is 5.3 mm, but the photoreceptor speed is reduced to 0.25 m/s. It is seen that the flow structure inside the corotron is quite complex with several vortices. The clockwise vortex on the left and central part becomes somewhat larger, while the counter-clockwise vortex on the right lower part become smaller and moves

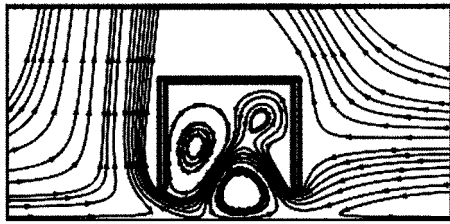


Figure 10. Stream traces for a case with wire voltage of 6000 V, substrate speed=0.5 m/s, and gap size=5.3 mm for an extended domain.

further to the right. The vortex on the right side of the corotron becomes larger and a smaller vortex forms at the middle bottom of the device. This figure also shows that air is sucked into the corotron from nearly the entire section of the outlet and moves on the top of the bottom vortex and leaves the corotron from the inlet section. Interestingly, at lower speed of 0.25 m/s, the viscous shear flow due to the photoreceptor motion, is entirely overwhelmed by the corona wind effect and little air is entering the corotron from the inlet side.

Figure 9(d) shows the stream traces for a case that the wire voltage is 6000 V, photoreceptor speed is 0.25 m/s, and the gap size is 2 mm. It is seen for a small gap size, the flow in the corotron is dominated by two large counter-rotating vortices on the right and left sides of the chamber. The air is drawn from the top part of the outlet section into the device and leaves that from the top part of the inlet section. The gap size appears to have an important effect on the flow structure in the corotron, while it does not have a noticeable effect on the electrical quantities.

To check the effect of the computational domain size and the boundary conditions used on the flow, a series of simulations were performed where the domain size was nearly doubled. The results are described in this section. Figures 10 and 11 show stream traces and the pressure distribution for the extended domain for a wire voltage of 6000 V, substrate speed of 0.5 m/s, and the gap size of 5.3 mm.

Figure 10 shows that the stream traces inside the corotron predicted for the extended domain are almost identical to those shown in Fig. 9(b). The stream traces on the left hand side of the device are, however, slightly different. Figure 11 shows the pressure distribution for the extended domain. It is seen that the pressure becomes constant near the outer boundaries which is as expected. The simulation results for the other cases in the extended domain have similar trend of behavior and therefore are not shown here.

The results were presented in this section show that the electrical quantities and the flow field in the corotron are strongly affected by the wire voltage and the substrate speed. The effect of gap size is important on the corotron flow but not on the electrical quantities.

## CONCLUSIONS

In this study the electric and the flow fields in a corotron under different operating conditions were analyzed. The

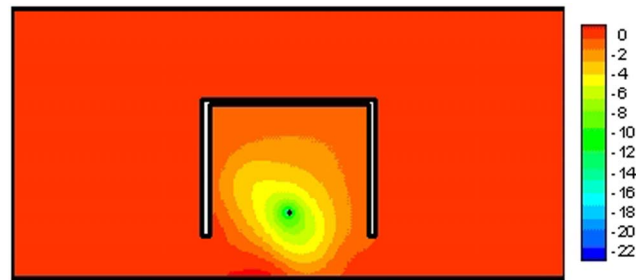


Figure 11. Pressure contours in Pa for a case with wire voltage of 6000 V, substrate speed=0.5 m/s, and gap size=5.3 mm with an extended domain.

simulations were performed using FIDAP™ commercial code with appropriate modifications. To account for the charge density variation on the wire that satisfies the Kaptsov's assumption and for the voltage boundary condition on the photoreceptor, two user-defined subroutines were developed and were implemented into the software. On the basis of the presented results, the following conclusions may be drawn:

- Increase of the wire voltage or decrease of the photoreceptor speed sharply increases the saturation charging of the photoreceptor surface.
- Increase of the wire voltage or increase of the photoreceptor speed increases the charge density current from the wire.
- Corona wind generates significant secondary flows in the corotron devices. The structure of the airflow varies depending on the wire voltage, photoreceptor speed and gap size.
- For the range of parameters studied in this work, the corona wind strongly affects the airflow conditions in the corotron, but the airflow effect on the electrical properties is relatively small.

Note that the nature of the contamination transport in the corotron under that action of airflow and electrostatic forces which is an important topic is not discussed in this paper due to space limitation. The subject, however, is under study and the results will be described in a future communication.

## ACKNOWLEDGMENTS

This work was supported by Xerox Corporation and by the New York State Office of Science, Technology and Academic Research (NYSTAR) (through the Center for Advanced Materials Processing, CAMP, of Clarkson University). The authors would also like to thank Fluent Inc. for making the FIDAP™ code available. Thanks are also given to IBM Corporation for the donation of pSeries computer to Clarkson University.

## REFERENCES

- <sup>1</sup>C. B. Duke, J. Noolandi, and T. Thieret, "The surface science of xerography", *Surf. Sci.* **500**, 1005–1023 (2002).
- <sup>2</sup>J. R. Macdonald, B. S. Wallace, H. W. Spencer III, and L. E. Sparks, "A

- mathematical model for calculating electrical conditions in wire-duct electrostatic precipitation devices", *J. Appl. Phys.* **48**, 2231–2243 (1977).
- <sup>3</sup>A. J. Medlin, C. A. J. Fletcher, and R. Morrow, "A pseudotransient approach to steady state solution of electric field-space charge coupled problems", *J. Electrostat.* **43**, 39–60 (1998).
  - <sup>4</sup>A. J. Medlin, R. Morrow, and C. A. J. Fletcher, "Calculation of monopolar corona at a high voltage DC transmission line with crosswinds", *J. Electrostat.* **43**, 61–77 (1998).
  - <sup>5</sup>G. A. Kallio and D. E. Stock, "Computation of electrical conditions inside wire-duct electrostatic precipitator using a combined finite-element, finite difference technique", *J. Appl. Phys.* **59**, 1799–1806 (1986).
  - <sup>6</sup>J. L. Davis and J. F. Hoburg, "VDC transmission line computations using finite element and characteristics methods", *J. Electrostat.* **18**, 1–22 (1986).
  - <sup>7</sup>K. Adamiak, "Adaptive approach to finite element modeling of corona fields", *IEEE Trans. Ind. Appl.* **30**, 387–393 (1994).
  - <sup>8</sup>Z. M. Al-Hamouz, "A combined algorithm based on finite elements and a modified method of characteristics for the analysis of the corona in wire-duct electrostatic precipitators", *IEEE Trans. Ind. Appl.* **38**, 43–49 (2002).
  - <sup>9</sup>G. Giovanni and R. D. Graglia, "Two dimensional finite boxes analysis of monopolar corona fields including ion diffusion", *IEEE Trans. Magn.* **26**, 567–570 (1990).
  - <sup>10</sup>X. Li, I. R. Ciric, and M. R. Raghuvver, "Investigation of ionized fields due to bundled unipolar DC transmission lines in presence of wind", *IEEE Trans. Power Deliv.* **14**, 211 (1999).
  - <sup>11</sup>G. W. Penney and R. E. Matick, "Potentials in D-C corona fields", *Trans. Am. Inst. Electr. Eng.* **79**, 91–99 (1960).
  - <sup>12</sup>G. L. Leonard, M. Mitchner, and S. A. Self, "An experimental study of the electrohydrodynamic flow in electrostatic precipitators", *J. Fluid Mech.* **127**, 123–140 (1983).
  - <sup>13</sup>T. Yamamoto and H. R. Velkoff, "Electrohydrodynamics in an electrostatic precipitator", *J. Fluid Mech.* **108**, 1–18 (1981).
  - <sup>14</sup>G. A. Kallio and D. E. Stock, "Interaction of electrostatic and fluid dynamic fields in wire-plate electrostatic precipitators", *J. Fluid Mech.* **240**, 133–166 (1992).
  - <sup>15</sup>J. Q. Feng, "Electrohydrodynamic flow associated with unipolar charge current due to corona discharge from a wire enclosed in a rectangular shield", *J. Appl. Phys.* **86**, 2412–2418 (1999).
  - <sup>16</sup>P. Zamankhan, G. Ahmadi, and F. Fan, "Coupling effects of the flow and electric fields in electrostatic precipitators", *J. Appl. Phys.* **96**, 7002–7010 (2004).
  - <sup>17</sup>J. Q. Feng, P. W. Morehouse, Jr., and J. S. Facci, "Steady state corona charging behavior of a corotron over a moving dielectric substrate", *IEEE Trans. Ind. Appl.* **37**, 1651–1657 (2001).
  - <sup>18</sup>*FIDAP User's Manual, Version 8.7* (Fluent Inc., Evanston, IL, 2003).
  - <sup>19</sup>N. A. Kaptsov, *Elektricheskie Yavleniya v Gazakh Vakuume* (OGIZ, Moscow, 1947).
  - <sup>20</sup>F. W. Peek, Jr., *Dielectric Phenomena in High Voltage Engineering* (McGraw-Hill, New York, 1929).
  - <sup>21</sup>O. C. Zienkiewicz and R. L. Taylor, *Finite Element Method: Volume 3, Fluid Mechanics* (Butterworth-Heinemann, London, 2000).
  - <sup>22</sup>I. Christie, D. F. Griffiths, A. R. Mitchell, and O. C. Zienkiewicz, "Finite element methods for second order differential equations with significant first derivatives", *Int. J. Numer. Methods Eng.* **10**, 1389–1396 (1976).